2025 MANDALAY EARTHQUAKE

RESEARCH ARTICLE

Direct estimation of earthquake source properties from a single CCTV camera

Soumaya Latour[1]†, Mathias Lebihain[2], Harsha S. Bhat[3], Cédric Twardzik[4], Quentin Bletery[4], Kenneth W. Hudnut[5], François Passelègue[4]*†

We present a direct measurement of the slip-rate function from a natural coseismic rupture, recorded on 28 March 2025, during the moment magnitude (M_w) 7.7 Mandalay earthquake (Myanmar). This measurement was made using video footage of the surface rupture captured by a closed-circuit television (CCTV) security camera located only meters away from the fault trace. Using direct image analysis, we measured the relative slip at each time step and deduced the slip rate. Our results show a local slip duration of 1.4 seconds and a cumulative slip of ~3 meters, during which surface slip velocity peaked at ~3.5 meters per second with passage of the rupture front. These findings demonstrate the pulse-like nature of the seismic rupture at the location of the recording. Using slip-pulse elastodynamic rupture models, we obtained the complete mechanical properties of this pulse, including the energy release rate.

Estimating the spatial and temporal evolution of slip along fault interfaces is critical for understanding the physics of deformation processes in Earth's crust throughout the seismic cycle (*1*). Because slip typically occurs at depth under extreme conditions, direct in situ observations are, in most cases, impossible. Reconstructions of slip history rely on inverse modeling (*2*). Consequently, our understanding of earthquake physics is fundamentally limited by the resolution and coverage of the data used in these inversions, as well as the inherent complexity of the forward problem (*3*–*6*). As a result, many key aspects of earthquake rupture, particularly the local dynamics of slip and the associated stress evolution at the fault interface, remain poorly constrained.

On 28 March 2025, a devastating moment magnitude (M_w) 7.7 earthquake struck Myanmar along the Sagaing fault (*7*) near Mandalay. The earthquake caused catastrophic damage: more than 5400 fatalities, >11,000 injuries, and hundreds to thousands reported missing. Infrastructure losses included 120,000 homes, 2500 schools, numerous temples, and key transportation networks such as bridges and airports. Several historic sites, particularly in Inwa, suffered extensive damage. This right-lateral strike-slip event ruptured more than 450 km of the fault, with slip reaching the surface on long segments and horizontal displacements up to 6 m [Fig. 1A; (*8*)]. The moment source function derived from the US Geological Survey (USGS) (*9*) indicates that the rupture propagation lasted ~120 s (Fig. 1B), in agreement with the SCARDEC solution (*10*), and likely included supershear phases (*11*).

Beyond its societal impact, the earthquake offered an unprecedented scientific opportunity: For the first time, a closed-circuit television (CCTV) security camera located just meters from the surface rupture captured the real-time deformation of the ground during seismic faulting (*12*). This footage provides a direct observation of coseismic surface displacement, enabling us to extract the time history of slip and slip rate at a specific fault point, measurements that, until now, were only accessible through laboratory experiments or inferred indirectly through modeling. In this study, we analyzed the footage to obtain a direct measurement of the slip-rate function during a natural earthquake (*13*) and, additionally, to invert the evolution of shear stress, energy dissipation (breakdown work), and rupture dynamics. Our results provide ground-truth constraints on seismic rupture physics, offering a critical benchmark for validating numerical models and seismic inversions and helping to close a long-standing observational gap in earthquake science.

Measurement of local slip rate during the earthquake

The camera was positioned on the east side of the fault and was approximately oriented in the southwest direction. To estimate the local slip rate, we tracked distinct visual landmarks located on both sides of the fault (Fig. 2A). The primary landmark was a concrete or metallic pillar ($R0$) located on the west side of the fault; two additional landmarks, $R1$ and $R2$, were small poles located adjacent to a road and behind a fence composed of vertical bars. Throughout the video, these features display predominantly horizontal motion relative to the foreground, consistent with right-lateral strike-slip faulting.

To quantify this motion, we defined two fault-parallel lines intersecting the vertical landmarks (Fig. 2A) and tracked the pixel intensity along these lines over the entire duration of the observable rupture propagation (Fig. 2, B to E). We defined $t = 0$ s as the approximate onset of fault slip [corresponding to the time stamp 12:46:34.633 of the video and not synchronized to universal time coordinated (UTC)]. Ground shaking began at $t = -4.5$ s, which is evident as coherent motion across the frame due to camera motion. A secondary seismic phase was observed at approximately $t = -1.8$ s. The onset of fault slip was identified as the moment when the tracked landmarks began to move relative to nearby, foreground features. This relative motion continued until approximately $t = 1.6$ s (Fig. 2C).

For each landmark, we selected a nearby visually stable reference point on the east side of the fault, as shown in Fig. 2A: $R0'$ (a vertical wall) and $R1'$ and $R2'$ (vertical bars of the fence). We tracked the motion of both the landmark and its corresponding reference feature over time (Fig. 2, C and E). The difference in their pixel positions provided a measure of relative displacement that was corrected for camera motion. We determined the temporal and spatial resolutions using the method described in the supplementary materials (fig. S1), and we applied a spatial scaling using an estimate of the final slip. This approach yielded a temporal resolution of 0.033 s and a spatial resolution with a relative uncertainty of approximately ±20%.

The slip history derived from the three measurements is shown in Fig. 3A. The curve obtained from $R0$ provides the most reliable estimate, as both the onset and arrest of motion were clearly visible in the video. The timing and slope of estimates from $R1$ and $R2$ are consistent with that of $R0$. The slip increased smoothly from 0 to 3 m over ~1.4 s, after which it ceased. We obtained the slip-rate function (Fig. 3B) by numerically differentiating the slip history after resampling it at 90 Hz. We then applied a moving average with a 0.33-s time window, as we interpreted the oscillations in the raw curve to result from uncertainties in manual tracking and camera-motion correction. The slip-rate function is slightly asymmetric: The slip rate rose rapidly from 0 to 3.5 m s^{-1} within 0.6 s, then decreased more gradually to 0 m s^{-1} over ~1 s. These values correspond to an average slip acceleration of 5.8 m s^{-2} and a slip deceleration of 3.5 m s^{-2}.

The total slip duration is best estimated using the rise time of the slip function, as the smoothing applied during signal processing tends to artificially broaden the slip-rate pulse. The most robust estimate of

[1]Université de Toulouse, CNRS, Observatoire Midi-Pyrénées, IRAP, Toulouse, France. [2]Navier, ENPC, Institut Polytechnique de Paris, Université Gustave Eiffel, CNRS, Marne-la-Vallée, France. [3]Laboratoire de Géologie, École Normale Supérieure, CNRS, UMR 8538, PSL Université, Paris, France. [4]Université Côte d'Azur, CNRS, Observatoire de la Côte d'Azur, IRD, Géoazur, Sophia Antipolis, France. [5]Southern California Edison, Rosemead, CA, USA. ***Corresponding author. Email: francois.passelegue@cnrs.fr** †These authors contributed equally to this work.

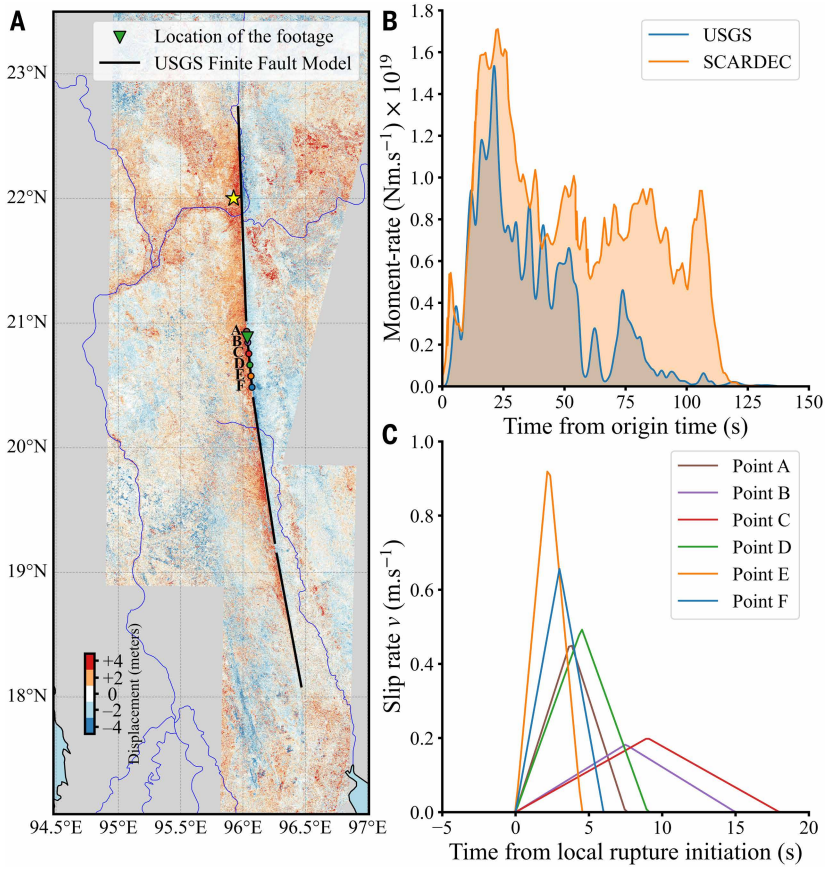

Fig. 1. Displacement field, moment-rate functions, and local slip-rate functions for the 2025 Mandalay earthquake. (**A**) North-south displacement field derived from the subpixel correlation of Sentinel-2 optical imagery. The yellow star indicates the location of the epicenter, and the green triangle marks the location of the footage, as given in the YouTube video description. The black lines show the surface trace of the finite fault model obtained from the USGS. Dots labeled A to F show the locations of the shallowest subfaults of the USGS finite fault model, which were used to extract the local slip-rate functions shown in (C). (**B**) Moment-rate functions from the USGS and SCARDEC. (**C**) Local slip-rate functions derived from the USGS finite fault model. This was only done for the shallowest subfaults of the segment highlighted in (A). Note that we use a triangular function to display the local slip-rate function instead of the asymmetric cosine function used by the USGS kinematic inversion.

slip duration is $\Delta t = 1.4$ s (Fig. 3A), independent of any assumptions related to spatial scaling. By contrast, our estimates of total and intermediate slip must consider a relative uncertainty of approximately ±20% in the spatial scaling factor. The uncertainty in total slip also affects absolute values of the slip rate.

Duration and shape of the slip-rate function

Our results highlight the much shorter local slip duration (1.4 s) compared with the total rupture duration of 100 to 120 s (Fig. 1B). This clearly shows that the rupture had a pulse-like nature, also called a self-healing pulse, at least at the surface along this segment of the fault. Self-healing pulses have long been identified as a possible mode of earthquake rupture (*14*). Indeed, pulse-like behavior appears to be a fairly common feature of rupture models for large earthquakes (*15*, *16*). The origin of this pulse-like behavior can be attributed to (i) the elongated geometry of the rupture or (ii) the structure of the fault damage zone (*17*). In the case of the Mandalay earthquake, the rupture was expected to have quickly saturated the seismogenic width, resulting in a large length-to-width ratio at the footage location. Under these conditions, it is expected that a pulse-like rupture would emerge naturally (*18*, *19*). However, alternative slip-healing mechanisms may also account for the short 1.4-s slip duration observed here. In particular, thermal pressurization of pore fluids within a thin gouge layer can induce rapid restrengthening behind the rupture tip. Using representative values for hydrothermal diffusivity ($\alpha = 10^{-4}$ to 10^{-6} m^2 s^{-1}) and a gouge thickness h ranging from 10^{-2} to 10^{-3} m (*20*, *21*), the expected slip duration scales to $\Delta t \approx h^2/\alpha \approx 1$ s (*22*), consistent with our observations. This mechanism does not rely on rupture aspect ratio and could explain the relatively small pulse width compared with the total rupture depth. Our results, however, are agnostic to various healing mechanisms simply because of the lack of additional in situ physical measurements.

The slip-rate values are consistent with the coseismic slip rates expected during large earthquakes. Particle velocity in the vicinity of the fault was predicted to be capable of reaching several meters per second for self-healing pulse ruptures (*14*). Note that our direct measurements of the fault slip rate are much higher than those estimated from inverted teleseismic data (*9*), which indicated a peak slip rate on the order of 0.2 m s^{-1} at the footage location (Fig. 1C). In addition, the recorded duration of local slip is much shorter than the inverted estimate: 1.4 s compared with ≈16 s for the USGS kinematic model. However, it is well known that modeling the rupture process involves substantial uncertainty (*6*, *23*). Indeed, the inverted slip duration just 10 km north of the footage location is much shorter (~6 s), and the peak slip rate is higher (0.45 m s^{-1}) (Fig. 1C). This discrepancy underscores the value of direct observation of slip during a natural earthquake as an empirical benchmark for validating and refining seismic source models of large earthquakes.

The shape of the slip-rate function is a key parameter in kinematic slip models (*24*) and plays an important role in ground motion prediction (*25*). In this study, the smoothed slip-rate function exhibits a simple form that can be described as an asymmetric triangle, with the duration of the acceleration phase being ~60% that of the deceleration phase. A similarly smooth, asymmetric, and triangular slip-rate function has been observed in friction experiments involving self-healing slip pulses propagating at 0.76 times the Rayleigh wave speed (*26*).

An analytical form of the slip-rate function was proposed for mode III self-healing pulses (*27*). This form, sometimes referred to as the Yoffe function, is characterized by an infinitely steep onset, a sharply peaked maximum, and a long tail with a variable slope. Although the Yoffe function qualitatively captures the asymmetry observed in our data, its overall shape is more peaked and strongly asymmetric. A regularized version of the Yoffe function, derived from dynamic rupture models (*28*), more closely resembles the slip-rate function observed in our measurements, though it still exhibits greater asymmetry.

Estimate of dynamic source parameters from the fault slip rate

We applied the elastodynamic equilibrium condition to infer the evolution of shear stress from a slip-based model. Assuming a two-dimensional plane strain shear (mode II) rupture propagating at a constant sub-Rayleigh rupture velocity V_r along the fault, the shear stress $\tau(x)$ is related to the spatial distribution of slip rate $v(x)$ through the singular integral equation (*22*, *29*, *30*)

$$\tau(x) = \tau_0 - \frac{\bar{\mu}}{2\pi V_r} PV \int_0^L \frac{v(\xi)}{x - \xi} d\xi \quad (1)$$

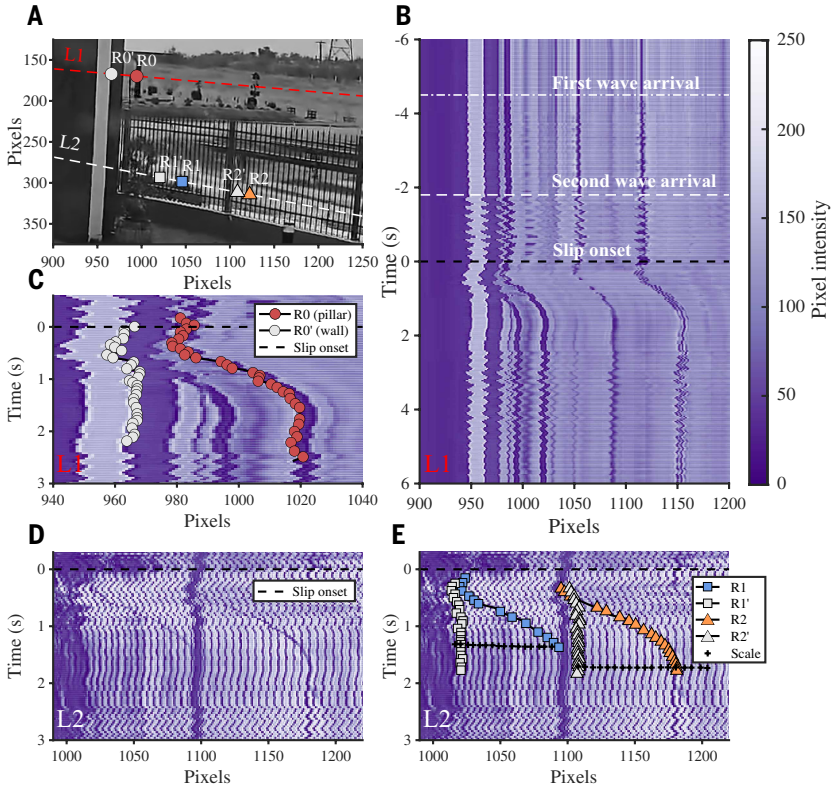

Fig. 2. Landmark tracking method. (**A**) Zoomed-in video frame showing tracked landmarks and their corresponding reference objects. The landmarks are as follows: *R0* (red circle) is the front-side pillar, *R1* (blue square) is the pole visible behind the fence, and *R2* (orange diamond) is the second pole behind the fence. The reference points are as follows: *R0′* (gray circle) is the arch wall, and *R1′* and *R2′* (gray square and diamond, respectively) are fence bars near the initial positions of *R1* and *R2*. The red dashed line (L1) indicates the axis used for projections in (B) and (C). The white dashed line (L2) indicates the axis used for projections in (D) and (E). (**B**) Motion tracking with annotations showing the arrival of the first seismic wave, second wave, and slip onset. (**C**) Pixel displacement time series for *R0* and *R0′*, measured along L1. (**D**) Pixel displacement time series for *R1*, *R1′*, *R2*, and *R2′*, measured along L2. (**E**) Same as (D), with additional annotations showing the tracking of each landmark and associated reference for *R1* and *R2* as well as a motion scale (black crosses).

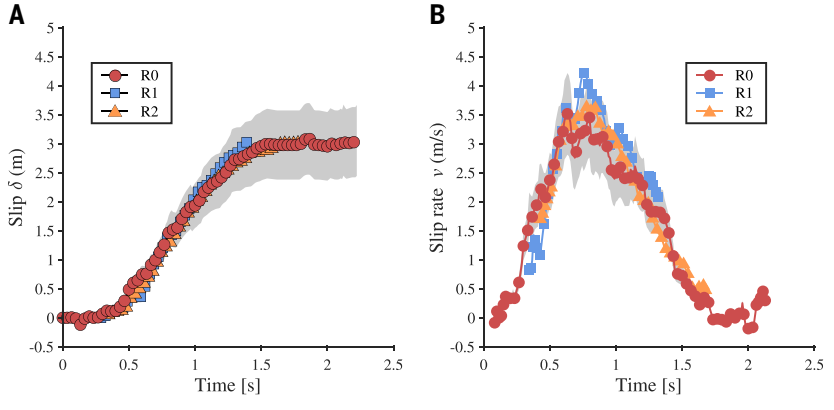

Fig. 3. Slip and slip-rate functions measured at the camera location. (**A**) Evolution of the fault slip during the rupture propagation modeled using the three landmark-reference pairs (Fig. 2A). (**B**) Slip-rate function derived from (A) for the three pairs. The gray shaded areas in (A) and (B) represent the effect of the 20% uncertainty in our slip estimate on the measurements derived from *R0*, which is the landmark used in the modeling. The symbols correspond to those described in Fig. 2.

where τ_0 is the background stress; $\bar{\mu}$ is a scaled shear modulus, which depends on the rupture velocity V_r; x is the distance to the rupture tip; $L = V_r\Delta t$ is the length of the slip pulse, which defines the spatial extent of the actively slipping region; ξ is the integration variable; and PV denotes the Cauchy principal value of the integral.

To compute the shear-stress evolution $\tau(x) - \tau_0$ along the fault, we interpolated $v(x)$ using a Chebyshev-based fit (Fig. 4, A and B), which captures the asymptotic behavior of slip and slip rate expected from fault mechanics, at both the leading and trailing edges of the pulse (see figs. S4 and S5 and supplementary materials for more details).

Once $v(x)$ was known, we inferred the shear stress evolution from Eq. 1 (Fig. 4C). Because the exact value of V_r was not known at this stage, we present results for two representative cases in Fig. 4C: $V_r/C_s = 0.75$ and $V_r/C_s = 0.90$. These ratios correspond to the two end-member rupture velocities of a rupture propagation scenario accounting for the ground motion and arrival times of the first and second seismic-wave arrivals as observed in the footage (Fig. 2B), implying a local sub-shear rupture velocity (see supplementary materials and fig. S3).

As anticipated for pulse-like ruptures, we observed that the stress drop was followed by a restrengthening phase (Fig. 4D) that spanned ~17% of the pulse length. The dependence of the shear-stress evolution on the rupture velocity V_r was also expected: A lower rupture velocity V_r requires a larger strength drop $\Delta\tau$, defined as the difference between the maximum and the minimum shear stress, to match the measured cumulative slip and slip rate. In addition, the size of the cohesive zone X_c, which corresponds to the distance over which the frictional strength of a fault degrades from its peak to residual level, increases linearly with V_r. Specifically, we found $\Delta\tau = 5.7$ MPa and $X_c = 3749$ m for $V_r = 0.90C_s$, compared with $\Delta\tau = 28.2$ MPa and $X_c = 3124$ m for $V_r = 0.75C_s$. Examining the apparent stress-slip relationship in Fig. 4D, we observed a decay of shear stress τ with slip δ, up to a critical slip value $D_c = 2.94$ m, which is consistent for both rupture velocities.

We then calculated the breakdown work $W_b = \int_0^{D_c} [\tau(\delta) - \tau_{min}]\,d\delta$ associated with the slip pulse, integrating up to the point of minimum stress τ_{min}, defined spatially at X_c and in cumulative slip at D_c (Fig. 4, C and D). Because this estimate is strongly dependent on final slip D_{fin} and rupture velocity V_r, we conducted a sensitivity analysis to characterize the uncertainty on these parameters (fig. S6 and supplementary materials). For the assumed final slip of 3.0 m, W_b ranges from 7.7 MJ m^{-2} for $V_r = 0.90C_s$ to 38.2 MJ m^{-2} for $V_r = 0.75C_s$.

To better constrain V_r and provide an independent direct measurement of the energy release rate G during the rupture pulse of the M_w 7.7 Mandalay earthquake, we fitted a classical two-dimensional steady-state rupture pulse model (*29*) to the observed slip pulse. The model assumes a steady-state sub-Rayleigh rupture velocity V_r and a constant-width cohesive zone in which the friction linearly decreases from the peak to the residual frictional strength ($f_p = 0.6$ and $f_r = 0.1$, respectively) behind the rupture front (fig. S7A). Unlike the direct slip-based model used previously, this model imposes a cohesive zone friction law and no healing within the pulse. Therefore, the energy released during

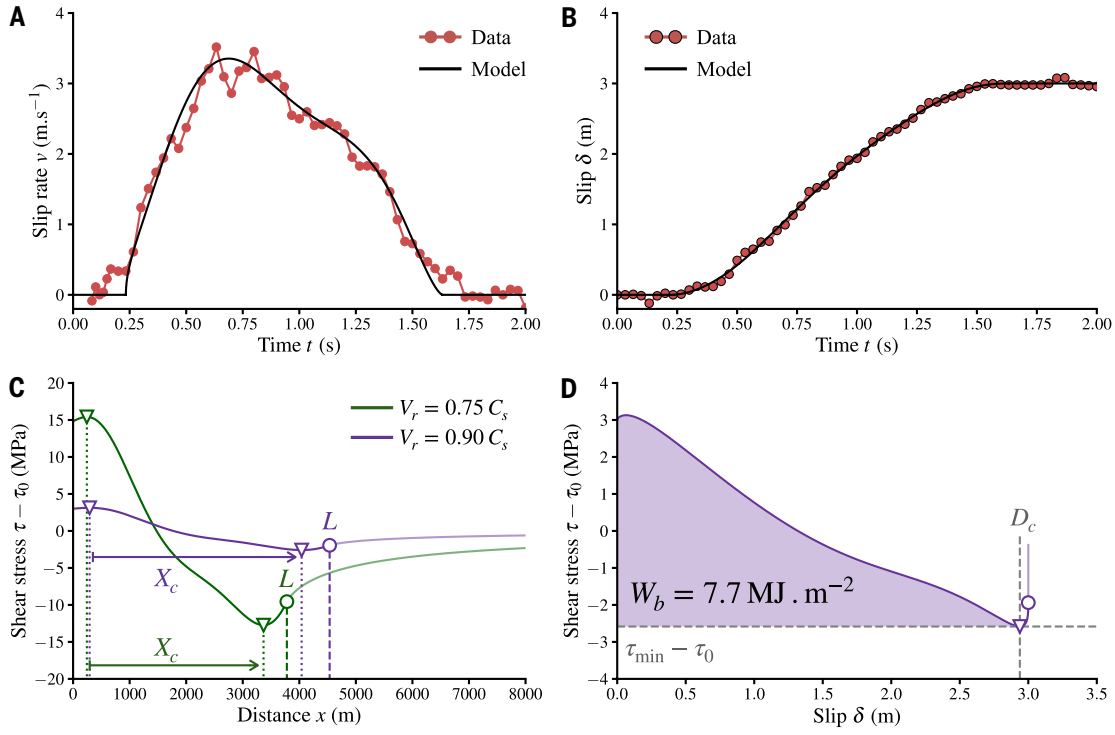

Fig. 4. Stress evolution and stress-slip relationship inferred from the slip-rate function. (**A** and **B**) Direct measurement (red circles) and Chebyshev-based fit (solid black curve) of (A) fault slip rate and (B) fault slip at the footage location. (**C**) Solution of the evolution of shear-stress change as a function of the distance from the rupture tip during slip-pulse propagation for rupture scenarios $V_r = 0.75C_s$ (solid green curve) and $V_r = 0.90C_s$ (solid purple curve). Cohesive zone size X_c is defined as the distance between the maximum and minimum of the shear-stress change (triangles), whereas the pulse length L corresponds to the extent of the actively sliding region (circles). (**D**) Evolution of stress variation $\tau - \tau_0$ with slip, including the healing stage for $V_r = 0.90C_s$. The breakdown work W_b (in shaded purple area) is defined from an integral of the shear-stress change $\tau - \tau_{min}$ up to the critical slip distance $\delta = D_c$.

the weakening contributes entirely to the rupture propagation and corresponds to G as described in fracture mechanics. Whereas the direct slip-based approach is applicable in this study because of the availability of true on-fault slip measurements from CCTV footage, the linear cohesive zone model is a more general framework that can be applied to conventional seismic observations, including data recorded at stations located away from the fault (*31*). We assumed a nominal normal traction of $\sigma_0 = 10$ MPa, consistent with the shallow nature of the rupture. The slip pulse duration was fixed at $\Delta t = 1.4$ s, as estimated previously. We performed a grid search on the scaled cohesive zone size to X_c/L and scaled rupture velocities V_r/C_s, identifying the parameters that produce the largest signal similarity index (SSI), which is a Euclidean-norm measure of how well the predicted slip-rate evolution matches that measured from image analysis. As seen in Fig. 5A, the optimal SSI corresponds to $X_c/L = 0.71$ and $V_r/C_s = 0.903$, which provides the fit of the curve in Fig. 5B. This X_c/L value is lower than the elastodynamic estimate of 0.83, as the pulse model prohibits restrengthening within the pulse, reducing the effective weakening (cohesive) zone. Nevertheless, the result supports $V_r = 0.90C_s = 3240$ m s^{-1} as the most consistent rupture scenario.

We have now obtained a complete mechanical characterization of the slip pulse observed in the CCTV data. The inferred strength drop was $\tau_p - \tau_r = 5$ MPa, the stress drop was $\tau_0 - \tau_r = 2$ MPa, and the corresponding slip-weakening distance was $X_c \approx 2.5$ m. These values are consistent with the slip-based model estimates ($\tau_p - \tau_r = 5.7$ MPa, $\tau_0 - \tau_r = 2.6$ MPa), except for $D_c = 2.94$ m, which was slightly overestimated because of the larger cohesive zone size. Ultimately, the energy release rate G was computed as $\int_0^{D_c} [\tau_f(\delta) - \tau_r] d\delta = 5.8$ MJ/m^2, where $\tau_f(\delta)$ is the strength evolution with slip δ (Fig. 5C). Assuming that $G = G_c$, our analysis here provides a direct estimate of the local fracture energy G_c of a natural fault. The energy release rate is of the same order of magnitude as our elastodynamic estimate of the breakdown work $W_b = 7.7$ MJ m^{-2}. Although related, the two quantities are not equivalent: G_c is expected to be smaller than W_b for ruptures that have undergone complete frictional weakening (*32*–*34*). Our value of G_c is consistent with expectations for an earthquake of the size and geometry of the Mandalay event (*35*–*38*), but it is substantially larger than values typically reported for experimental faults, both in analog materials (*39*, *40*) and in crustal rock samples (*41*, *42*). This difference is primarily attributed to the larger slip-weakening distance D_c inferred here, compared with the much smaller values typically observed during laboratory earthquakes (*40*, *41*). Nevertheless, such large values of D_c remain compatible with those measured during high-velocity friction experiments under upper-surface stress conditions (*43*–*45*) and are expected from seismic kinematics inversion of large earthquakes (*46*). Beyond the specific case of the Mandalay earthquake, these direct measurements offer a rare, empirical benchmark for earthquake source modeling. Unlike traditional kinematic and dynamic inversions, which are limited by data coverage and modeling assumptions, the video-derived slip and slip-rate functions provide ground-truth constraints on the physical processes behind large earthquakes, such as fault weakening, energy dissipation, and rupture dynamics.

Discussion

Our study highlights the potential for a new observational approach in earthquake science: strategically deploying CCTV or high–frame rate cameras near active, shallow-fault zones. Such installations could capture not only rapid, coseismic fault slip, as demonstrated here, but also slower aseismic deformation or postseismic creep. Compared with

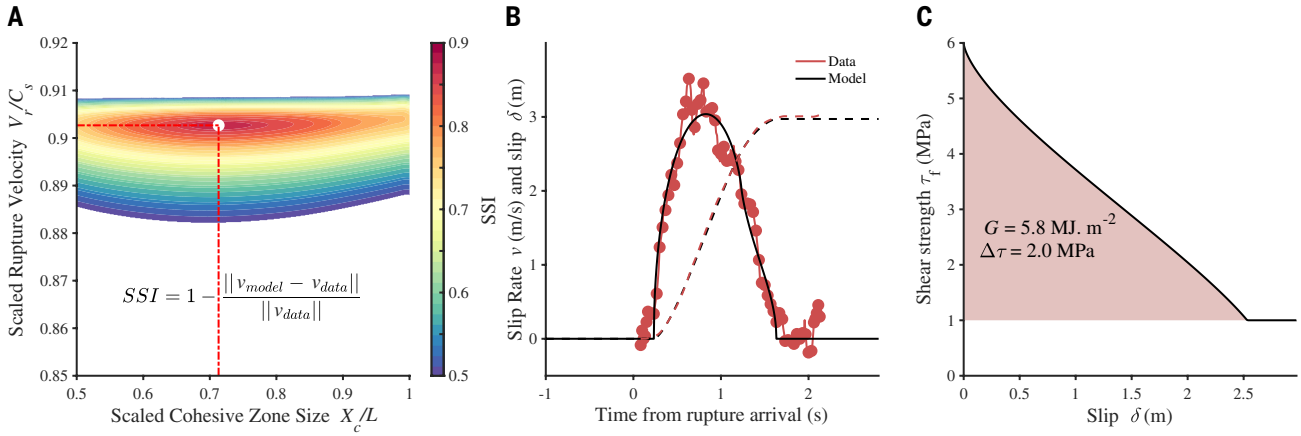

Fig. 5. Evaluation of rupture velocity and energy release rate. (**A**) Grid search for the best-fitting scaled cohesive zone size, X_c/L, and scaled rupture velocity, V_r/C_s. The fit is measured using the SSI, as defined in the text. v_{model} and v_{data} are slip rates from the model and the data, respectively. (**B**) Comparison of slip (dashed lines) and slip rate (solid lines) between the observed and best-fitting model slip pulse. (**C**) Evolution of friction strength, τ_f, with slip, δ.

traditional instrumentation such as broadband seismological stations or continuous GPS networks, video monitoring systems are relatively low cost, widely available, and easy to deploy, making them an attractive complementary tool for expanding fault-monitoring capabilities. With appropriate placement and calibration, these instruments could provide direct, high-resolution constraints on fault behavior across the full spectrum of slip modes, opening new avenues for studying earthquake physics.

REFERENCES AND NOTES

1. J.-P. Avouac, *Annu. Rev. Earth Planet. Sci.* **43**, 233–271 (2015).
2. A. Tarantola, B. Valette, *Rev. Geophys.* **20**, 219–232 (1982).
3. A. Saraò, S. Das, P. Suhadolc, *J. Seismol.* **2**, 1–25 (1998).
4. I. A. Beresnev, *Bull. Seismol. Soc. Am.* **93**, 2445–2458 (2003).
5. S. Hartzell, P. Liu, C. Mendoza, C. Ji, K. M. Larson, *Bull. Seismol. Soc. Am.* **97**, 1911–1934 (2007).
6. P. M. Mai *et al.*, *Seismol. Res. Lett.* **87**, 690–708 (2016).
7. G. Bertrand, C. Rangin, *J. Asian Earth Sci.* **21**, 1139–1157 (2003).
8. N. G. Reitman *et al.*, Remote surface rupture observations for the M7.7 2025 Mandalay, Burma (Myanmar) earthquake. USGS Data Release (2025); https://doi.org/10.5066/P1RYMWCK.
9. US Geological Survey, Finite Fault – M 7.7 - 2025 Mandalay, Burma (Myanmar) earthquake (2025); https://earthquake.usgs.gov/earthquakes/eventpage/us7000pn9s/finite-fault [accessed 16 May 2025].
10. M. Vallée, J. Charléty, A. M. Ferreira, B. Delouis, J. Vergoz, *Geophys. J. Int.* **184**, 338–358 (2011).
11. N. Inoue *et al.*, *Seismica* **4**, 1 (2025).
12. H. Richter, "Watch an earthquake split a hillside in two," *Science*, 22 July 2025.
13. J. Kearse, Y. Kaneko, *Seismic Record* **5**, 281–288 (2025).
14. T. H. Heaton, *Phys. Earth Planet. Inter.* **64**, 1–20 (1990).
15. D. Melgar, G. P. Hayes, *Geophys. Res. Lett.* **44**, 9691–9698 (2017).
16. V. Lambert, N. Lapusta, S. Perry, *Nature* **591**, 252–258 (2021).
17. F. Barras, E. Aharonov, F. Renard, *Geophys. Res. Lett.* **52**, e2024GL111189 (2025).
18. H. Weng, J.-P. Ampuero, *J. Geophys. Res. Solid Earth* **124**, 8584–8610 (2019).
19. H. Weng, J.-P. Ampuero, *Nat. Commun.* **13**, 7327 (2022).
20. J. R. Rice, *J. Geophys. Res. Solid Earth* **111**, B05311 (2006).
21. A.-A. Gabriel, D. I. Garagash, K. H. Palgunadi, P. M. Mai, *Science* **385**, eadj9587 (2024).
22. D. I. Garagash, *J. Geophys. Res. Solid Earth* **117**, B04314 (2012).
23. S. Minson, M. Simons, J. Beck, *Geophys. J. Int.* **194**, 1701–1726 (2013).
24. H. N. Razafindrakoto, P. M. Mai, *Bull. Seismol. Soc. Am.* **104**, 855–874 (2014).
25. I. A. Beresnev, *Pure Appl. Geophys.* **181**, 1859–1869 (2024).
26. G. Lykotrafitis, A. J. Rosakis, G. Ravichandran, *Science* **313**, 1765–1768 (2006).
27. S. Nielsen, R. Madariaga, *Bull. Seismol. Soc. Am.* **93**, 2375–2388 (2003).
28. E. Tinti, E. Fukuyama, A. Piatanesi, M. Cocco, *Bull. Seismol. Soc. Am.* **95**, 1211–1223 (2005).
29. J. R. Rice, C. G. Sammis, R. Parsons, *Bull. Seismol. Soc. Am.* **95**, 109–134 (2005).
30. N. Brantut, D. I. Garagash, H. Noda, *J. Geophys. Res. Solid Earth* **124**, 8998–9020 (2019).
31. E. M. Dunham, R. J. Archuleta, *Bull. Seismol. Soc. Am.* **94** , S256–S268 (2004).
32. F. Paglialunga, F. Passelegue, M. Lebihain, M. Violay, *Earth Planet. Sci. Lett.* **626**, 118550 (2024).
33. D. S. Kammer *et al.*, *Nat. Commun.* **15**, 4736 (2024).
34. B. Fryer, M. Lebihain, C. Noel, F. Paglialunga, F. Passelègue, *J. Mech. Phys. Solids* **193**, 105876 (2024).
35. R. E. Abercrombie, J. R. Rice, *Geophys. J. Int.* **162**, 406–424 (2005).
36. E. Tinti, P. Spudich, M. Cocco, *J. Geophys. Res. Solid Earth* **110**, B12303 (2005).
37. S. Nielsen *et al.*, *J. Seismol.* **20**, 1187–1205 (2016).
38. M. Cocco *et al.*, *Annu. Rev. Earth Planet. Sci.* **51**, 217–252 (2023).
39. I. Svetlizky, J. Fineberg, *Nature* **509**, 205–208 (2014).
40. F. Paglialunga *et al.*, *Earth Planet. Sci. Lett.* **584**, 117442 (2022).
41. D. S. Kammer, G. C. McLaskey, *Earth Planet. Sci. Lett.* **511**, 36–43 (2019).
42. S. Xu, E. Fukuyama, F. Yamashita, *J. Geophys. Res. Solid Earth* **124**, 766–787 (2019).
43. A. Tsutsumi, T. Shimamoto, *Geophys. Res. Lett.* **24**, 699–702 (1997).
44. T. Hirose, T. Shimamoto, *J. Geophys. Res. Solid Earth* **110**, B05202 (2005).
45. G. Di Toro *et al.*, *Nature* **471**, 494–498 (2011).
46. T. Mikumo, K. B. Olsen, E. Fukuyama, Y. Yagi, *Bull. Seismol. Soc. Am.* **93**, 264–282 (2003).
47. F. Passelègue *et al.*, Data and model for Direct Estimation of Earthquake Source Properties from a Single CCTV Camera. Zenodo (2025); https://doi.org/10.5281/zenodo.16785672.

ACKNOWLEDGMENTS

We thank those who uploaded and shared the analyzed footage on social media. F.P. thanks B. Fryer, N. Calza, and F. Paglialunga for discussions and for proofreading the manuscript. S.L. and F.P. thank J.-P. Ampuero and F. Courboulex for valuable discussions. We thank D. Garagash and an anonymous reviewer for their constructive remarks, which helped to enhance this paper. **Funding:** F.P. acknowledges support from the European Union (ERC Starting Grant HOPE, no. 101041966). H.S.B. acknowledges support from ERC Consolidator Grant PERSISMO (no. 865411) for partial support of this work. Q.B. acknowledges support from ERC Starting Grant EARLI (no. 949221) for partial support of this work. **Author contributions:** S.L. and F.P. conceived the study; S.L. and K.W.H. conducted the frame analysis based on satellite imaging; M.L. developed the elastodynamic inversion; F.P., H.S.B., and M.L. estimated the rupture properties; C.T. and Q.B. analyzed the kinematic inversion from USGS and provided estimates of the wave speeds; S.L. and F.P. wrote the first draft of the manuscript; and K.W.H. provided critical data for spatial scaling and validation. All authors contributed to discussions, interpretation of results, and review of the manuscript. **Competing interests:** The authors declare no competing interests. **Data and materials availability:** All data and code necessary to directly reproduce our results are available online at Zenodo (*47*). This research was funded in whole or in part by ERC (101041966, 865411, and 949221); as required the author will make the Author Accepted Manuscript (AAM) version available under a CC BY public copyright license.

SUPPLEMENTARY MATERIALS

science.org/doi/10.1126/science.adz1705
Supplementary Text; Figs. S1 to S7; References (*48*–*54*)

Submitted 20 May 2025; accepted 29 August 2025

10.1126/science.adz1705